This is the peer-reviewed version of:

Mastilovic S. *A PD simulation-informed prediction of penetration depth of rigid rods through materials susceptible to microcracking.* <u>Meccanica **57** (12): 3051–3069, (2022).</u> Springer Nature.

A PD simulation-informed prediction of penetration depth of rigid rods through materials susceptible to microcracking

Sreten Mastilovic[*]

University of Belgrade, Institute for Multidisciplinary Research, Kneza Viseslava 1, 11030 Belgrade, Serbia

Abstract

The present investigation relies upon an alternative approach to estimate the penetration depth of rigid projectiles into quasibrittle materials that utilizes simulation-informed modeling of penetration resistance. Penetration at normal incidence of a long rigid rod into massive targets, made of materials with inferior tensile strength predisposed to microcracking, is an event characterized by a high level of aleatory variability and epistemic uncertainty. This inherent stochasticity of the phenomenon is addressed by a model developed based on the particle dynamics (PD) simulations aimed to provide a key modeling ingredient – the functional dependence of the radial traction at the cavity surface on the radial velocity of the cavity expansion. The penetration depth expressions are derived for the ogive nose projectiles. The use of the power law radial traction dependence upon the expansion rate yields the penetration resistance and depth equations defined in terms of hypergeometric functions. These expressions are readily evaluated and offer a reasonably conservative estimate of the penetration depth. This model is validated by using experimental results of the penetration depth of long projectiles into Salem limestone, which is a typical example of quasibrittle materials with random microstructure well known for their pronounced experimental data scatter. This stochasticity is explored in the present paper by a sensitivity analysis of the key input parameters of the model; most notably, uniaxial tensile strength and friction coefficient.

1 Introduction

Studies of projectile penetration into geological targets are usually focused on the penetration depth or deceleration history. Analytical modeling of the high-velocity penetration through a quasibrittle solid is beset with inherent complexities coupled with a dearth of detailed experimental insight into underlying physical mechanisms. These complexities tend to obscure identification of the important physical quantities especially in the case of the quasibrittle materials well known for the pronounced scatter of experimental data. A typical penetration event is characterized by large deformations at extremely high strain rates, encompassing inertia effects, complex patterns of stress- and failure-wave propagations, mass transport and phase transitions; all taking place within a few microseconds. The material in the target-projectile contact zone is melted within a thin contact layer, the target material is pulverized in the immediate vicinity of the emerging penetration tunnel, and inundated by microcracks forming complex damage patters dependent upon the impact energy and the distance from the tunnel. The shattered and fragmented material is transported away from the projectile path by the fragment cloud energetically ejected from the crater. The process is, for all practical purposes, adiabatic. A rational model of penetration must recognize these salient features of the phenomenon and incorporate their effects.

Penetration mechanics is a mature research field with vast amount of literature accumulated over the past several decades. A concise review is conducted recently by Anderson [1] enveloping the most-influential analytical models that include rigid-body and eroding penetration, both steady-state and transient. Warren and coauthors [2] offer a succinct survey of experiments and simulations with emphasis on rocks. The solution technique advanced in the present study belongs to the category of

---

[*]**Corresponding author:**
Email: misko.mastilovic@imsi.bg.ac.rs, Tel: +381 64 2360-444, ORCID ID: 0000-0002-1856-626X

theoretical models that approximate response of the semi-infinite target by one-dimensional motion using cavity-expansion methods [3-5]. Following the work of Hopkins [5], a number of authors employed this approach to develop analytical models for penetration problems (e.g., [6-9]). Extensive reviews of related studies are available in [10, 11]. The cavity expansion theories are constantly re-examined, from various points of view, to improve agreement with experimental results. For example, Kong and coworkers [11] used the cavity expansion approximation to develop eroding projectile penetration model into mortar targets. Johnsen and coauthors [12] employed the cylindrical cavity expansion (CCE) using three different strain hardening models for the class of materials characterized by the growth of ductile holes as the primary damage-evolution mechanism. Zhang and colleagues [13] used the Tresca law for description of the fragmented region around the expanding cavity to investigate the penetration depth into concrete targets. Notably, Warren [14] examined applicability of the cavity expansion approximation for modeling the rigid penetration. A debate that issued with regards to the use of target inertia is summarized vividly in Anderson's review article [1]. It suffices herein to reiterate Warren's conclusion that penetration depth predictions for rigid decelerating projectiles (based on the cavity expansion approximation that includes target inertia) are in excellent agreement with the experimental data for aluminum targets for the wide range of striking velocities, various projectile materials and nose geometries [14].

The present study is different in a sense that it utilizes the particle dynamics (PD) simulations of a dynamic CCE to estimate the radial traction required to facilitate the cavity growth at a prescribed rate. The dependence of the radial traction on the cylindrical cavity surface (σ_r) on the CCE velocity (v_r) is not available from the experimental investigations. Thus, the functional dependence $\sigma_r = f(v_r)$ is traditionally assumed to be quadratic (by analogy with dynamic pressure) based on the curve fitting on numerical results or closed-form solutions obtained from the cavity expansion theories for different constitutive models of target materials (e.g., [1], [11], [12]). The present investigation examines the possibility—suggested by the results of the PD simulations of CCE in a generic highly-brittle material susceptible to microcracking—that the term associated with the CCE velocity v_r might be in the form of a more general power law rather than the quadratic form. Key contributors to PD simulation-driven modeling are the verification, model validation, and quantification of uncertainty due to parameter sensitivity. This modeling approach is originated by Mastilovic and Krajcinovic [15, 16] and substantially extended herein in terms of both computational and analytical effort. Most notably, the extended range of CCE velocities explored by the PD simulations, highlights the nonlinearity of the response at the high-velocity end, lacking in the original studies.

Finally, due to versatility of various topics addressed in the present article, some remarks that would ordinarily belong to introduction are postponed to the following sections to facilitate discussion and presentation flow.

2 Computer simulation technique

Particle models represent one of many attempts to bridge the gap between the spatial scales. The PD, utilized in the present study, can be envisioned as a generalization of spring network models with dynamic effects included and can also be considered an engineering offshoot of molecular dynamics (MD) on a coarser spatial scale ("quasi-MD" [17]). The choice of the coarser spatial scale implies that the role of atoms/molecules is being taken over by "continuum" particles or quasi-particles mimicking a larger chunk of material. Other than that, the adopted computational PD model has the traditional MD techniques at the root.

This model was used extensively in the past and described and explored in detail in literature (e.g., [15]). Krajcinovic and coworkers [15, 18-23] demonstrated that the present PD model can be used to determine changes of thermodynamic states during non-uniform and non-equilibrium deformation processes. Thus, only a succinct summary should suffice herein. The current approach is based on the equivalence between an ideal two-dimensional hexagonal lattice and a three-dimensional elastic continuum under plane-strain conditions ([15] and references therein), which makes the present PD technique well suited to simulate CCE. The system consists of N material points of known masses m_i, and positions r_i ($i = 1,…, N$), arranged randomly in accordance with a Delaunay simplicial graph (illustrated in Fig. 1) dual to a honeycomb system of Voronoi polyhedra. These material particles may

represent different micro/meso-constituents (e.g., rock clasts, ceramic grains, concrete aggregates) that govern macro response of the discontinuous and/or heterogeneous material system characterized by low fracture energy. Each bulk particle, associated with a node of an underlying irregular, two-dimensional network, is linked initially to its six nearest neighbors (Fig. 1) by "chemical" bonds that are strongly nonlinear in compression and linear in tension prior to the steep rupture [15]. The choice of this simple central-force interaction renders the total elastic deformation energy of the system dependent exclusively on the mutual distances among particles, $r_{ij} = r_j - r_i \ (= r$; hereinafter for brevity). The computer simulation technique requires solution of the system of differential equations of motion of the system of particles with defined momenta, which are approximated by an appropriate system of finite differences and then solved using one of the many available algorithms [20]. In order to increase the speed of program execution, it is useful to make and maintain a list of neighbors for each particle in accordance with the common MD practice.

The hybrid potential:

$$\varphi^r\left(\bar{r}\right) = \frac{k\,r_0^2}{(B-2)}\left(\frac{1}{B}e^{B(1-\bar{r})} - \bar{r}^{-1}\right), \ \bar{r} < 1 \tag{1a}$$

$$\varphi^a\left(\bar{r}\right) = \frac{1}{2}k\,r_0^2\left(\bar{r}-1\right)^2, \ \bar{r} \geq 1 \tag{1b}$$

is a combination of Born-Mayer (1a) and Hookean (1b) potentials. In Eqs. (1a, 1b), superscripts r and a denote, respectively, the repulsive and attractive branch of the interaction; $\bar{r} = r / r_0$, with subscript 0 referring to the reference configuration and indices (i, j) marking interacting particles dropped for brevity. Also, the average bond stiffness is proportional to the modulus of elasticity ($\bar{k} = 8\sqrt{3}\,E_0 / 15$), while the steepness of the repulsive wall parameter B can be selected, for example, by matching the ballistic equation of state [18]. Obviously, in this case, the parameters of the interparticle potential are selected by considering the behavior of the material on macro scale (top-down approach [20]). Watson and Steinhauser [24] recently devised a similar particle potential to model hypervelocity impact of aluminum spheres into a fixed thin plate with a notable difference that, instead of the Born-Mayer potential, a "more ductile" Leonard-Jones 6-12 potential is used in the nonlinear repulsive branch, Eq. (1a).
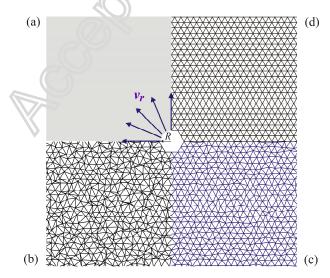

Fig. 1 (a) Detail of schematics of the PD simulation of the CCE with the radial velocity v_r. Examples of the effect of geometrical disorder on the particle-associated lattice: (b) $\zeta_r = 0.001$ (the maximum disorder within the present PD simulation framework), (c) $\zeta_r = 0.5$, and (d) $\zeta_r = 1$ (the ideal lattice). (The current cavity radius is marked by R; its change during CCE is $\Delta R = R - R_0 = \Delta\bar{R} \cdot \bar{r}_0$; the lattice nodes represent locations of particles while the short lines between them depict interparticle forces.)

The resulting force-elongation relation ($f = -d\varphi/dr$)—linear with tensile cut-off in the attractive and nonlinear in the repulsive branch—was proved capable to capture some salient features of the deformation process typical of the considered quasi-brittle materials subjected to dynamic loading such as: brittle tensile behavior, increase in shock wave velocity and decrease in compressibility with increasing pressure [15].

Modeling of microstructural randomness and concomitant stochastic damage evolution is crucial for the model ability to capture the essence of penetration phenomenology. In general, the quenched disorder introduced into the particle network may be topological (unequal coordination numbers among particles, z), geometrical (unequal interparticle distances, r_0; Fig. 1), or structural (unequal bond strengths and/or stiffnesses, k). In the present PD model, the geometrical and structural disorders were, respectively, introduced by the normal distribution of the reference-configuration interparticle distances (r_0) and the uniform distribution of the corresponding bond stiffnesses (k)— $\left\lfloor \varsigma_{r|k} \cdot \bar{r}_0 \big| \bar{k} \leq r_0 \big| k \leq \left(2 - \varsigma_{r|k}\right) \cdot \bar{r}_0 \big| \bar{k} \right\rfloor$—with their bandwidths defined by the geometrical (ζ_r) and structural (ζ_k) disorder parameters such that $0 < \zeta_{r|k} < 1$ [15]. The rupture of interparticle bond was defined by the critical elongation $\varepsilon_{cr} = (r_{cr} / r_0 - 1)$. The mean critical link elongation is the model parameter that can be determined from the uniaxial tensile testing of the material. It cannot be overemphasized that this inherent aleatory variability of the quasibrittle material system is further enhanced by the damage evolution governed, in turn, by the local fluctuations of stress acting upon the quenched energy barriers.

The present PD model recognizes two different types of interparticle interaction: chemical and mechanical. The chemical bonding is limited to nearest neighbors while the number of particles interacting by mechanical bonding is unlimited. The healing of a microcrack is prevented by ruling out the establishment of the attractive force between two particles that were not linked initially or were separated at some point in the process of deformation by the rupture of the link that kept them together. However, the repulsive force *can* be established between two particles, which were originally not linked together[1] or, were separated beyond the critical limit. Thus, the repulsive interaction can be either chemical or mechanical as opposed to the attractive interaction that is solely of the former kind. The formation of the repulsive force between the particles that were not connected initially by cohesive forces is *essential* to model the cataclastic flow of the fragmented rock that is of crucial importance for the CCE modeling.

Computer simulations of the cavity nucleation and its dynamic growth are conceptually simple. The cavity is nucleated at the middle of the underlying particle network. After that, all particles on the cavity surface are driven radially outward at a prescribed expansion rate (Fig. 1a). The size of the particle system increased three times (≈ 34000 particles) compared to the original studies [15, 16] while its geometric and structural parameters are the same: the average (mean) equilibrium distance between particles $\bar{r}_0 = 1$, the average link stiffness $\bar{k} = 50$, the geometrical disorder parameter $\zeta_r = 0.001$ (the maximum disorder illustrated in Fig. 1b), the structural disorder parameter $\zeta_k = 0.6$, and the critical (fracture) strain $\varepsilon_{cr} = 0.1\%$. (The maximum geometrical disorder and the small fracture strain are selected with aim to capture behavior of a highly brittle material.) The comparison of the key PD simulation results, the radial traction time histories, obtained for various values of ε_{cr}, ζ_k and ζ_r is shown in Fig. 4.

Finally, if the interaction of a system of particles can be approximated by the central-force potential, the expression for the components of the stress tensor

$$\sigma_{\alpha\beta} = \frac{1}{2\Lambda} \sum_{\substack{i,j \\ j \neq i}} \frac{d\varphi}{dr_{ij}} \frac{(r_{ij})_\alpha (r_{ij})_\beta}{|r_{ij}|} = -\frac{1}{2\Lambda} \sum_{\substack{i,j \\ j \neq i}} f_{ij} \frac{(r_{ij})_\alpha (r_{ij})_\beta}{r_{ij}} \tag{2}$$

can be adopted from statistical mechanics (e.g., [18, 20, 25] and references therein). In Eq. (2) Λ is the averaging-region area, while $(r_{ij})_\alpha$ and $(r_{ij})_\beta$ are the α and β components of the distance vector $\boldsymbol{r}_{ij}$ between particles i and j. The stress expression (2), based solely on the interparticle-force term, is a

---

[1] that were not initially the nearest neighbors and, consequently, not chemically bonded but brought together by the mass transport (and the resulting compressive forces) accompanying CCE.

proven valid measure of mechanical stress at the scale of the small set of particles, which can be identified with the Cauchy stress [25].

The approximation of a quasibrittle solid by an ensemble of particles interacting via the nonlinear potential is selected for a number of reasons. First, the random microstructure of the subject materials, characterized by morphological and structural disorder, is straightforwardly incorporated. Second, the selection of the constitutive relations capturing the essential physics can be, in principle, inferred from the molecular models (bottom-up approach [20, 22]). Third, procedures to achieve the rigorous mapping of the geometrical and structural (elastic) properties of a disordered polycrystalline microstructure into a particle network are developed and validated by Rinaldi and coauthors [19]. Finally, there is no need to develop ingenious, time-consuming computational techniques to track the material interfaces.

3 General expressions for the penetration resistance of long rigid projectiles

A long rigid projectile with an ogive nose (Fig. 2) impacts the target at normal incidence with striking velocity v_s and continues to penetrate it with velocity v_z ($v_s \geq v_z \geq 0$). For the rigid projectile, the motion history and penetration depth can be calculated if the penetration resistance force is known. The penetration resistance derivation in this section is based on the target approximation by thin independent layers of material perpendicular to the penetration direction (emphasized by the gray-shaded areas in Fig. 2), which facilitates the use of the CCE theory.

The ogive nose geometry is defined by the caliber radius head

$$\psi = \frac{s}{2a} = \frac{1}{4}\left[1 + \left(\frac{l}{a}\right)^2\right] \tag{3}$$

where l is the projectile nose length, and a is the shank radius as indicated on Fig. 2a.

Note that the use of CCE is inherently more suitable for modeling the "sharper" ogive-nose projectiles characterized by larger caliber-radius-head values (3), which are better approximated by the plane-strain conditions than those with blunter nose that are better suited for the use of the spherical cavity expansion models. Since the target is idealized as a stack of thin material layers, the penetration resistance is determined by the radial force necessary to dynamically open the cylindrical cavity. The equality of elementary works necessary to perform this task provides the following relationship
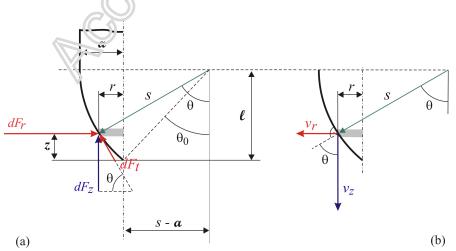

Fig. 2 Geometry of the ogive nose projectile and corresponding penetration parameters. The forces and velocities correspond to the radial (r) and tangential (t) directions with respect to the ogive nose contour while those in the penetration direction are marked with subscript z. The sketches emphasize the axial symmetry of the problem and the CCE approximation (v_r, F_r).

$$dF_z = dF_r \frac{dr}{dz} \tag{4a}$$

If the elementary force, Eq. (4a), necessary to open a cylindrical cavity, is augmented by the elementary resistance force due to the sliding friction (assumed in the form $dF_t = \mu\,\sigma_r\,dA$), the elementary penetration resistance is

$$dF_z = \sigma_r\,(2\pi r\,dz)\frac{dr}{dz} + (\mu\,\sigma_r)(2\pi r\,s\,d\theta)\sin\theta \tag{4b}$$

Note that within the CCE approximation, the radial traction σ_r, responsible for the penetration resistance, consequently provides the far-field compression at the contact interface for the frictional resistance. This treatment of friction is consistent within the CCE framework and falls within the overall epistemic uncertainty in the frictional resistance, which is discussed in detail in the present study.

From the ogive nose geometry, illustrated in Fig. 2, it follows that

$$r = (a-s) + \sqrt{s^2 - (l-z)^2} \quad \Rightarrow \quad \frac{dr}{dz} = \frac{l-z}{\sqrt{s^2 - (l-z)^2}} \tag{5}$$

It is also convenient to introduce the following relationships:

$$\sin\theta_0 = 1 - \frac{1}{2\psi}, \quad \cos\theta_0 = \frac{\sqrt{4\psi-1}}{2\psi} \tag{6}$$

Consequently, Eq. (4b) could be expanded in the following form:

$$dF_z = 2\pi(a - s + \sqrt{s^2 - (l-z)^2})\,\frac{l-z}{\sqrt{s^2 - (l-z)^2}}\,\sigma_r(v_z,z)\,dz + $$
$$+ 8\,a^2\pi\,\psi^2\,\mu\,(\sin\theta - \sin\theta_0)\sin\theta\,\sigma_r(v_z,\theta)\,d\theta \tag{7}$$

and integrated

$$F_z = 2\pi\int_0^l (a - s + \sqrt{s^2 - (l-z)^2})\,\frac{l-z}{\sqrt{s^2 - (l-z)^2}}\,\sigma_r(v_z,z)\,dz + $$
$$+ 8\,a^2\pi\,\psi^2\,\mu\,\int_{\theta_0}^{\pi/2}(\sin\theta - \sin\theta_0)\sin\theta\,\sigma_r(v_z,\theta)\,d\theta \tag{8}$$

The evaluation of the integrals appearing in Eq. (8) requires an analytical form of the traction at the projectile nose, $\sigma_r(v_z,\theta)$, that resists penetration. Usually, the analytical form of this traction is obtained from a one-dimensional, symmetric analysis of a cavity expansion (spherical or cylindrical). As already mentioned, in the present study the analytical form of the radial traction is deduced based on the information provided by the CCE PD simulations summarized in the following section.

4 The PD-informed modeling of the radial traction dependence upon the CCE velocity

The CCE PD simulations provide a functional dependence of the radial traction on the cavity surface, σ_r, on the cavity expansion velocity, v_r, that is depicted by square symbols in Fig. 3.

The abovementioned set of simulation results is enlarged substantially in the present study, compared to the original set [15], with additional expansion-velocity simulations performed with a larger PD model. It cannot be overemphasized that these additional simulations affect the key modeling inputs not only quantitatively but also qualitatively.

First, the additional simulations confirm the original observation of the linear $\bar{\sigma}_r = \sigma_r/K$ vs.

6

$\bar{v}_r = v_r / C$ dependence in the medium-to-high CCE velocity range ($\bar{v}_r \in [0.0135, 0.20]$), which is defined by the slope $(1 - \upsilon)/(1 + \upsilon)$ as illustrated in Fig. 3 and Eq. (9). (Where K, C and υ denote, respectively, the bulk modulus, velocity of longitudinal elastic wave propagation and Poisson ratio of the pristine material.) It is not inconceivable that this more-or-less pronounced quasi-linearity of the $\bar{\sigma}_r = f(\bar{v}_r)$ mid-range is a feature distinguishing the brittle materials (with the random microstructure and inferior tensile strength predisposed to microcracking) from the ductile materials.

The PD simulation results shown in Fig. 3 are obtained from the radial traction time histories illustrated in Fig. 4 (due to the controlled-displacement loading, time scales with the change of cavity radius presented on abscissas). All σ_r time histories are characterized by a steep stress jump to a very large magnitude, followed by a more-or-less rapid (depending on the loading rate) decline and, eventually, a relaxation into a saturation state (obviously, the steady-state in terms of a "long" time average). Figs. 4b-4d indicate that the peak and the saturation (steady-state, stagnation) radial traction values are practically not affected by the choice of the PD model input parameters (the link rupture strain, ε_{cr}; structural disorder parameter, ζ_k; and geometrical disorder parameter ζ_r).

The abovementioned σ_r slope (depicted by the dashed line in Fig. 3) stems from the noted regularity of the radial traction histories (Fig. 4):

$$\bar{\sigma}_r^{lb} = \frac{1}{3}\bar{\sigma}_r^F = \frac{1}{3}\left[\frac{3(1-\upsilon)}{(1+\upsilon)}\bar{v}_r\right] = \left(\frac{1-\upsilon}{1+\upsilon}\right)\bar{v}_r \tag{9}$$

that, fortuitously or not, relates the discerned low-bound stress value ($\bar{\sigma}_r^{lb}$) with the radial stress at the elastic wave front at the cavity edge ($\bar{\sigma}_r^F$) derived by Krönm [4]. Mastilovic and Krajcinovic [15] noted that $\bar{\sigma}_r^F$ (marked by a solid black circle at the ordinate of the radial traction time histories presented in Fig. 4) captures with uncanny accuracy the value of the σ_r initial jump.
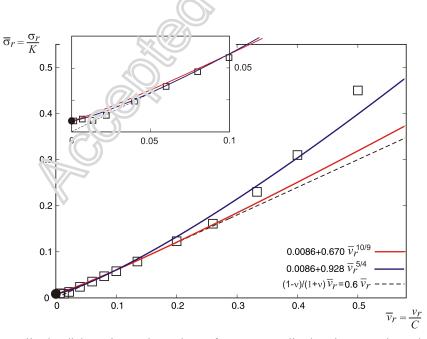

Fig. 3 Normalized radial traction at the cavity surface vs. normalized cavity expansion velocity. The square symbols mark the substantially expanded set of CCE PD simulation results originally presented by Mastilovic and Krajcinovic [15]. The black circle at the ordinate corresponds to the radial traction necessary to expand cavity statically; $(\bar{\sigma}_r)_{st}$, defined by Eq. (11a). The lines represent two different analytical curves modeling the data, which are discussed in Appendix A.
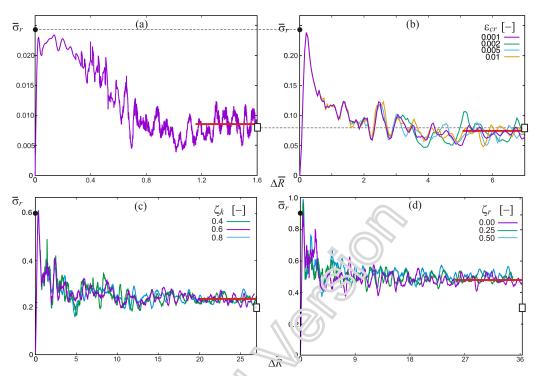
Fig. 4 Radial traction at the cavity surface vs. change of the cavity radius (normalized values) for four widely different cavity expansion velocities (v_r/C): (a) 0.0135, (b) 0.135, (c) 0.33 and (d) 0.50. The black circles on the ordinates mark the values corresponding to the analytical solutions of the radial stress at the elastic wave front at the cavity edge $\bar{\sigma}_r^F$ [4]. The empty rectangles on the right correspond to the one-third of the peak stresses, given by Eq. (9), and approximate reasonably well the stagnation (steady-state) values of the radial traction in the medium-to-high expansion velocity range [0.0135, 0.20] marked by the thick red lines. For the highest expansion velocities, $v_r > 0.2 \cdot C$, the steady-state radial tractions deviate from the one-third rule of thumb and $\bar{\sigma}_r = f(\bar{v}_r)$ exhibits pronounced nonlinearity. The change of cavity radius on abscissa scales with time. (The curve sets at Fig. 4b-d illustrate results of the sensitivity analysis of the radial traction time histories with respect to the change of the PD input parameters: the link rupture strain, ε_{cr}; structural disorder parameter, ζ_k; and geometrical disorder parameter ζ_r. The upper plots highlight the proportionality of the peak and the steady-state radial tractions.)

Importantly, the additional simulations indicate that the steady-state (saturation) radial-traction values eventually deviate from the one-third rule of thumb (9) in the range of the highest expansion velocities ($v_r > 0.20 \cdot C$), which is evident from Figs. 4c-d. Consequently, pronounced nonlinearity of the functional dependence $\bar{\sigma}_r = f(\bar{v}_r)$ emerges[2].

It cannot be overemphasized that the radial traction functional dependence on the CCE velocity, $\bar{\sigma}_r = f(\bar{v}_r)$, suggested by Fig. 3, is the key ingredient to the penetration resistance expression (8) in the preceding section. In the original article [15] (that overlooked the nonlinearity in the high velocity range), this functional dependence has been analytically represented by two approximations: (i) the bilinear, and (ii) the second-order parabola. The obvious problem with the bilinear approximation (in

---

[2] This nonlinearity is reminiscent of the pressure - particle velocity curves observed in the shock physics. This is not just a coincidence, since, within the present PD framework, σ_r and v_r indeed represent the internal pressure at the cavity surface and the radial velocity of the corresponding particles.

8

addition to the "non-smoothness") is that it underestimates the radial traction for the high expansion velocities ($v_r > 0.20 \cdot C$) since the nonlinearity passed unnoticed originally due to the narrower CCE velocity range explored. The problem with the parabolic approximation (that is commonly used in analytical modeling) is that it likely overestimates radial tractions for the larger expansion velocities *if* the characteristic slope in the medium-to-high expansion velocity range is to be accounted for in the model in the manner described in Appendix A.

In the present study, the functional dependence of the radial traction on the radial velocity of the CCE is assumed in the following form

$$\bar{\sigma}_r = \mathcal{B} + \mathcal{A} \cdot \bar{v}_r^{\gamma}, \quad \gamma \in \Re^+, \gamma > 1 \tag{10}$$

The derivation of model parameters

$$\mathcal{B} = \left(\bar{\sigma}_r\right)_{st} = \sqrt{\frac{3(1-2\upsilon)}{(1+\upsilon)(3-2\upsilon)}\left(\frac{\sigma_f}{K}\right)} \tag{11a}$$

$$\mathcal{A} = \frac{\alpha^{1-\gamma}}{\gamma}\left(\frac{1-\upsilon}{1+\upsilon}\right)^{\gamma}\left(\bar{\sigma}_r\right)_{st}^{1-\gamma} \tag{11b}$$

$$\gamma = \frac{\alpha}{\alpha-1} \quad \Leftrightarrow \quad \alpha = \frac{\gamma}{\gamma-1} \tag{11c}$$

is presented in Appendix A.

Succinctly, $\mathcal{A}$ and γ are obtained from requirement that the radial traction curve (10), approaching from above, touches the lower bound (9) at $\alpha \cdot \bar{v}_r^*$ (where $\alpha > 1$) as shown in Fig. 8 of Appendix A. In Eq. (11a), $\left(\bar{\sigma}_r\right)_{st}$ marks the radial traction at the cavity surface corresponding to the static CCE, while σ_f designates the indirect tensile strength associated with the elastic-cracked response [15, 16].[3] An example of different sets of parameters (11a-11c) corresponding to the functional dependence (10) is left for Appendix A.

Obviously, the larger values of the exponent γ capture better the nonlinearities corresponding to the small-velocity and the high-velocity regions; the smaller γ values naturally flatten the curve and, thus, favor its linear-like appearance in the medium-to-high velocity region (i.e., the function (10) "comes closer" to the inclined lower bound (9); Fig. 3). It is evident that a compromise between these two conflicting requirements (the quasi-linearity in the medium-to-high, and the nonlinearity in the high, velocity region) is necessary in order for ansatz (10) to reproduce the PD simulation results. Therefore, Fig. 3 suggests that a reasonable overall agreement with the PD simulation results is achieved with exponent $\gamma = 5/4$ that departs from the observed radial traction at $\bar{v}_r \approx 0.5$ (which is, for example, over 2000 m/s for Salem limestone used in the numerical examples to follow).

Finally, it should be noted that, in engineering applications involving massive targets made of quasibrittle solids, the power law exponent γ is an independent parameter ($1 < \gamma \leq 2$). The actual choice of the value of this model parameter is a problem-specific task, but it is clear that the impression of quasi-linearity of the $\bar{\sigma}_r = f(\bar{v}_r)$ mid-range is increasingly difficult to retain for $\gamma \geq 3/2$. The target inertia for ductile metals is usually proportional to v^2 by analogy to the resistance term of the traditional fluid mechanics (e.g., Poncelet equation [1]). The PD simulation results suggest the working assumption that the exponent $\gamma < 2$ might be more convenient for the rigid penetration of the materials susceptible to microcracking characterized by inherently less ductile dynamic response.

---

[3] Despite the importance of the tensile strength in controlling failure processes on all micro/meso scales, it is often overlooked recently in engineering practice in general, and the penetration modeling in particular, due to difficulties with obtaining reliable experimental data. Be it as it may, the fracture initiation in materials characterized by low fracture energy is dominantly a *tensile* phenomenon on the spatial scale that dominates macro-response regardless of the sign of the far-field loading.

5 Calculations of the penetration depth based on the PD-informed modeling of the radial traction dependence upon the CCE velocity

The penetration resistance acting on the ogive nose is defined by the integral expression (8). Thus, upon the substitution of the radial traction (10) into Eq. (8), and evaluation of the integrals, the following analytical form of this force is derived

$$F_z = \alpha_{co} + \beta_{co}\, \bar{v}_z^{\gamma} \tag{12a}$$

$$\alpha_{co} = \lambda_{co}\, (\bar{\sigma}_r)_{st} \left[1 + 4\psi^2\, \mu\left(\frac{\pi}{2} - \theta_0 + \frac{1}{2}\sin 2\theta_0\right)\right], \quad \lambda_{co} = a^2 \pi K \tag{12b}$$

$$\beta_{co} = 8\lambda_{co}\, \psi^2 A \left\{ \begin{aligned} & \frac{(\cos\theta_0)^{\gamma+2}}{\gamma+2}\left[{}_2F_1\left(\frac{\gamma}{2}, 1+\frac{\gamma}{2}, 2+\frac{\gamma}{2}, \cos^2\theta_0\right) - (1-\frac{1}{2\psi})\, {}_2F_1\left(\frac{1+\gamma}{2}, 1+\frac{\gamma}{2}, 2+\frac{\gamma}{2}, \cos^2\theta_0\right)\right] + \\ & + \mu\left[\frac{(\cos\theta_0)^{\gamma+1}}{\gamma+1}\left({}_2F_1\left(\frac{1}{2}, \frac{1+\gamma}{2}, \frac{3+\gamma}{2}, \cos^2\theta_0\right) - \sin\theta_0\right) - \frac{(\cos\theta_0)^{\gamma+3}}{\gamma+3}\, {}_2F_1\left(\frac{1}{2}, \frac{3+\gamma}{2}, \frac{5+\gamma}{2}, \cos^2\theta_0\right)\right] \end{aligned} \right\} \tag{12c}$$

where $_2F_1$ $(a, b; c; f(z))$ designates the hypergeometric function (e.g., [26])

The expressions for parameters α_{co} and β_{co} may appear cumbersome but they are unambiguously determined by the material properties (K, v, σ_f), the ogive nose geometry (a, ψ), and the sliding friction coefficient (μ) and can be readily evaluated.

The penetration resistance expression (12a) is then substituted into Newton's second law of motion

$$m_p \frac{dv_z}{dt} = -F_z \quad \Rightarrow \quad m_p C^2 \int_0^{\bar{v}_s} \frac{\bar{v}_z}{(\alpha_{co} + \beta_{co}\, \bar{v}_z^{\gamma})} d\bar{v}_z = \int_0^{D} dz \tag{13}$$

and the evaluation of the integrals in Eq. (13), eventually yields the penetration depth in the form

$$D = \frac{KE}{\alpha_{co}} \cdot {}_2F_1\left(\frac{\gamma}{2}, 1, 1+\frac{\gamma}{2}, -\frac{\beta_{co}}{\alpha_{co}}\left(\frac{v_s}{C}\right)^{\gamma}\right) \quad KE = \frac{m_p\, v_s^2}{2} \tag{14}$$

where m_p stands for the projectile mass, v_s – the striking velocity and KE – the kinetic energy of the impacting projectile.

The proportionality between the penetration depth of the ogive nose projectile and its kinetic energy at impact is observed frequently in empirical formulas [27].

6 Numerical examples for the penetration depth of the rigid ogive-nose projectiles

The present model is validated by using a set of ballistics tests in which Salem limestone targets were impacted by rigid ogive-nose projectiles having different sizes [28, 29]. It is obvious from Eq. (14) and the expressions for the corresponding parameters (12b-c) that, in addition to the striking velocity, the penetration depth of the rigid ogive-nose projectiles is dependent upon:
- projectile data (m_p – projectile mass, a – shank radius, ψ - caliber radius head);
- target material properties (K – bulk modulus, v – Poisson ratio, σ_f – splitting tensile strength);
- sliding friction coefficient (μ);
- power-law exponent ($\gamma \leftrightarrow \alpha$).

The physical and mechanical material properties of quasibrittle materials are well known for their extremely pronounced scatter (e.g., [30, 31]). This aleatory variability may have far-reaching consequences on engineering applications in general, and the model validation in particular, since it is unlikely that all necessary inputs are reported in experimental penetration studies while compilation of the material properties from different sources is an iffy endeavor.

The material properties of the Salem limestone used herein ($K = 26.5$ MPa, $\upsilon = 0.23$, $C = 4280$ m/s, and $\sigma_f = 9$ MPa) are compiled from the experimental penetration study by Frew and coauthors [29] and the triaxial compression experiments by Green [32] and Crosby [33]. It should be noted that the indirect (splitting) tensile strength σ_f is, out of necessity, *estimated* based on the uniaxial compressive strength $\sigma_c = 75$ MPa [32] and 72.3 MPa [33]. The σ_f choice naturally affects the calculation results and the necessity to use this stochastic and extrinsic property, difficult to objectively determine experimentally, needs to be investigated. The tensile strength of the quasibrittle materials susceptible to microcracking is typically an order of magnitude inferior to the uniaxial compressive strength. The limestone penetration studies rarely even report σ_f while the available experimental data suggest values from $\sigma_c/10$ to $\sigma_c/7$ [31]. Moreover, the value $\sigma_f = 9$ MPa is suggested by the recently-developed empirical correlation formula between the unconfined compressive strength and the indirect tensile strength of limestone rock samples, $\sigma_f = (\sigma_c \, [\text{MPa}]/9.25)^{1/0.947}$ [31]. Clearly, the uncertainty remains; as an example, Frew et al. [29] report a range of lower σ_c values from 58 MPa to 67 MPa, while the estimate of σ_f based on σ_c is a source of uncertainty in itself. Rosenberg and collaborators [43] associate the different compressive strengths of limestone to the well-known size effect in rocks.

The comparisons of the penetration depth predictions (14) based on the newly-developed model (Eqs. (10) and (11a-c)) and the experimental data on the penetration depth of the ogive-nose projectiles into the Salem limestone targets [28, 29] are presented in Tables 1 and 2 and Figs. 5 and 6. The agreement between the experimental and computational results is reasonable keeping in mind that the estimate is based *solely* on the elastic material properties and the tensile strength obtained under the static loading conditions. Nonetheless, it should not be overlooked that the PD model, regardless of its simplicity, is capable to capture some subtle features of the high-rate response of the quasibrittle materials such as the adiabatic elastic moduli [21], the damage evolution and corresponding patterns [15, 22, 23], the cataclastic flow [16]. Actually, based on Fig. 5, it seems that the largest differences between results at a few striking velocities—specifically, (a) 853 m/s and 1134 m/s, and (b) 939 m/s and 1098 m/s—are more likely than not due to the experimental uncertainty. (Relatively large striking-velocity increases that result in comparably modest penetration-depth increases.) Nevertheless, the calculation-results sensitivity to some stochastic input parameters may cast a shadow on the model applicability if left unexplored.

6.1 Parametric sensitivity of calculation results

The sensitivity of calculation results with respect to the choice of key model-input parameters is investigated as shown in Tables 1 and 2.

First, the value of the exponent γ determines: (i) the "closeness" of the $\bar{\sigma}_r \left(\propto \bar{v}_r^{\gamma} \right)$ curve to the linear inclined lower bound, and (ii) the degree of the nonlinearity in the high-velocity range (Fig. 3). The selection of smaller value of the exponent, $\gamma = 10/9$, results in a less nonlinear $\bar{\sigma}_r = f(\bar{v}_r)$ and, consequently, a smaller penetration resistance for the higher striking velocities. Nonetheless, the large difference between the two curves should emerge only at relatively high radial expansion velocities ($v_r > 0.4 \cdot C \approx 1600$-$1700$ m/s for Salem limestone), which is beyond the velocity range used herein for validation and parametric sensitivity study. Consequently, the comparison of the calculation results in the 3rd (corresponding to $\gamma = 5/4$) and 4th ($\gamma = 10/9$) columns of Tables 1 and 2, shows that the difference becomes pronounced only at the higher striking velocities (roughly, $v_s > 1000$ m/s) as expected. Overall, although the results are not too sensitive within the explored γ range, the fact remains that in engineering applications γ represents an independent model parameter that may take larger ($1 < \gamma \le 2$) values than those suggested by the PD simulation results (Fig. 3).

On the other hand, the tensile strength reduction (from $\sigma_f = 9$ MPa to $\sigma_f = 6$ MPa) results in the 12% increase of the penetration depth on average, for both small-size (Table 1) and medium-size (Table 2) projectiles. The difference in results is relatively uniformly distributed over the entire explored striking-velocity range. This σ_f effect appears acceptable bearing in mind the overall uncertainty of the penetration depth estimate.

Table 1. Comparison of the test and computational results for penetration of a small-size ogive-nose projectile (m_p = 0.117 kg, $2a$ = 12.7 mm, ψ=3.0; Table 1 of ref. [28]) into Salem limestone targets.

v_s	D^{exp}	$\gamma=5/4$ $D_{\mu=0.08}^{\sigma_f=9\text{MPa}}$	$\gamma=10/9$ $D_{\mu=0.08}^{\sigma_f=9\text{MPa}}$	$\gamma=5/4$ $D_{\mu=0.08}^{\sigma_f=6\text{MPa}}$	$\gamma=5/4$ $D_{\mu=0.02}^{\sigma_f=9\text{MPa}}$
[kg/m³]	[m]	[m]	[m]	[m]	[m]
459	0.141	0.156	0.153	0.181	0.192
608	0.232	0.254	0.252	0.291	0.310
853	0.362	0.445	0.448	0.504	0.543
956	0.523	0.535	0.543	0.603	0.652
1134	0.562	0.703	0.720	0.787	0.853
1269	0.812	0.838	0.866	0.935	1.016
1404	0.924	0.980	1.021	1.090	1.188
1502	1.017	1.087	1.139	1.206	1.316

Table 2. Comparison of the test and computational results for penetration of a medium-size ogive-nose projectile (m_p = 0.61 kg, $2a$ = 25.4 mm, ψ=3.0; Table 2 of ref. [28]) into Salem limestone target.

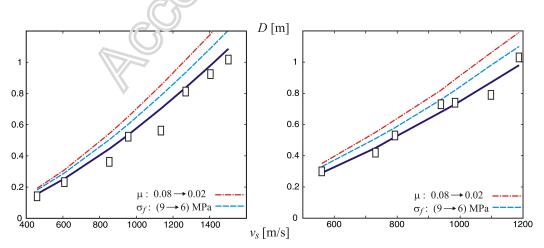| v_s	D^{exp}	$\gamma=5/4$ $D_{\mu=0.08}^{\sigma_f=9\text{MPa}}$	$\gamma=10/9$ $D_{\mu=0.08}^{\sigma_f=9\text{MPa}}$	$\gamma=5/4$ $D_{\mu=0.08}^{\sigma_f=6\text{MPa}}$	$\gamma=5/4$ $D_{\mu=0.02}^{\sigma_f=9\text{MPa}}$
[kg/m³]	[m]	[m]	[m]	[m]	[m]
560	0.30	0.29	0.28	0.33	0.35
731	0.42	0.45	0.45	0.51	0.55
793	0.53	0.52	0.52	0.58	0.63
939	0.73	0.68	0.69	0.76	0.82
984	0.74	0.73	0.74	0.82	0.89
1098	0.79	0.87	0.89	0.98	1.06
1184	1.03	0.98	1.01	1.10	1.19

Fig. 5. Dependence of penetration depth on striking velocity. Comparison of experimental (rectangles) and computational results for penetration of: (a) small-size (Table 1) and (b) medium-size (Table 2) ogive-nose projectile into Salem limestone targets. (Note that the solid lines correspond to the basic set of computational set of results - 3rd columns in Tables 1 and 2, while the dashed blue lines and the dash-dotted red lines correspond to the 5th and 6th columns, respectively.)

12

The noticeable *tendency* of the present model to overestimate the penetration depth could, at least to some extent, be attributed to the neglect of the peak of the $\bar{\sigma}_r = f(\bar{v}_r)$ curve in the derivation of the penetration resistance (recall the radial traction time histories of Fig. 4 and the use of steady-state values in Fig. 3). More importantly, it could be attributed to the use of the CCE approximation that is estimated by Bishop, Hill and Mott [3] to result in approximately 15% lower resistance pressure at a conical indenter compared to the spherical cavity approximation. The same authors suggested that "the pressure on a lubricated punch deep in a material" is likely to be somewhere in between the two approximations with general tendency to lean toward the CCE with increase on the nose sharpness (specifically, the caliber radius head ψ for the ogive nose projectile). (An appropriate correction factor could be introduced easily into the radial traction expression (10) to account for this uncertainty.)
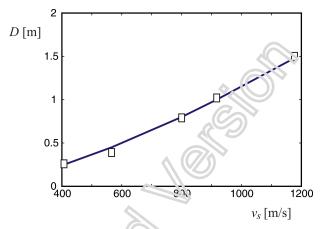

Fig. 6. Dependence of penetration depth on striking velocity. Comparison of the test and computational results for penetration of a large-size ogive-nose projectile (m_p = 0.931 kg, $2a$ = 25.4 mm, ψ=3.0; Table 4 of ref [29]) into Salem limestone targets.

6.2 Sensitivity to sliding friction

The obvious importance of the sliding friction on the penetration depth is discussed from the very onset of the penetration studies [3] to the present [34, 35]. These deliberations are to this day hampered by lack of experimental techniques that can quantify the frictional phenomena at the high sliding velocities. Early on, Forrestal and Grady [36] set the friction coefficient value to μ = 0.08, based on the data available at the time. Not long after, Forrestal and coworkers [37] explored the friction coefficient values 0.02 and 0.10 for the rigid penetration into 6061-T651 aluminum targets. In these early studies, the frictional resistance was introduced hypothetically to bring the analytical models in agreement with the experimental data [39]. Importantly, Hill suggested in retrospect, that the frictional component of the penetration resistance can be "disregarded because of surface melting" [40], which effectively promotes the contact lubrication (see the closing remarks in Appendix B). The physical soundness of this intuitive suggestion was confirmed by detailed and complex finite element analysis by Camacho and Ortiz [41] (matched against the aluminum armor penetration experiments) that indicated a very thin melted layer in the target-projectile contact zone that resulted in a practically frictionless interface. Recently, the frictional resistance is neglected frequently (e.g., [12, 38]) but not entirely. As an example, a study of Jiang and coauthors [35] on the role of friction in rigid penetration into concrete-like materials, resulted in the observation that below a certain critical striking velocity adding friction improves the agreement with the experimental data; while, with the rise in striking velocity, the sliding friction effect weakens to the extent that it can be ignored. Numerical results obtained from various engineering models developed in the last two decades ([34, 35] and references therein), continue to deliberate on the dependence of the friction coefficient on the sliding velocity and suggest that the friction coefficient, after all, could be a legitimate ingredient into

the penetration models. Be it as it may, Anderson [1] concluded not long ago that "when an accurate constitutive model is used, there is no need to include friction for ballistic penetration modeling."

Nonetheless, it cannot be overemphasized that the penetration depth estimate (14) rests on PD simulation results (Fig. 3) based on the constitutive modeling [15] that can be classified as semi-quantitative rather than accurate in the abovementioned sense. Therefore, it seems appropriate to investigate herein to what extent the choice of the friction coefficient affects the ability of this simple model to reproduce the experimental data. The approach is twofold.

6.2.1 Constant friction coefficient

First, two relatively-small values of the friction coefficient μ are selected for this sensitivity study (0.08 and 0.02). These values are then applied over the whole striking velocity range (Tables 1 and 2). The μ reduction caused the penetration depth increase of 20.0% and 21.4% on average for the two projectile sizes, respectively.[4] The observed penetration-depth difference is perhaps not alarming, bearing in mind the reduction of the friction coefficient by the factor of four, but (since both values used are relatively small) it reaffirms that the choice of this parameter should not be taken lightly. Moreover, as discussed above, with the increase of the striking velocity, the value of the sliding friction coefficient tends to zero, which highlights the importance of judicious use of the model given by Eqs. (14) and (12a-c). The present model needs to account for frictional resistance in order to reproduce the experimental data accurately.

6.2.2 Velocity-dependent friction coefficient

Second, it is recognized that, at low striking velocities, the use of the constant friction coefficient throughout the entire penetration process is an iffy approach in itself (see Appendix B). On one side, penetration starts with the initial striking velocity ($v_z = v_s$) and ends with the projectile arrest ($v_z \equiv 0$). On the other side, at any moment of the penetration process (at any given penetration velocity) the sliding velocity varies from the minimum value at the tip of the projectile nose to the maximum at the nose-shank transition. For example, for $v_z = 250$ m/s and the ogive nose with $\psi = 3.0$, the sliding velocity at the nose varies within the range [181, 250] m/s. Thus, to explore the effect of this range of different velocities, a simplified analytical model is developed in Appendix B, able to include the friction coefficient that changes with the sliding velocity. Fig. 7a offers comparison of the two simplified analytical models developed in Appendix B corresponding to the friction coefficient that is treated as a constant, Eq. (28), or the velocity-dependent, Eq. (30), as illustrated in Fig. 9a. It should be noted that the two abovementioned penetration depth expressions are derived under the restrictive assumption of the linearized $\bar{\sigma}_r = \bar{\sigma}_r^{lb} = f(\bar{v}_r)$ dependence—Eq. (26)—which neglects the quasistatic resistance and the significant deviation from the linear lower the high-velocity range. Therefore, the comparison in Fig. 7a is meant *solely* to emphasize the effects of the velocity-dependent treatment of the friction coefficient compared to the use of the constant value (i.e., the calculation results among themselves) and the experimental data is added only for the illustrative purpose.

Thus, the comparison of the results corresponding to the constant μ calculations (the blue dash-double dotted line for 0.02 and the red dashed line for 0.08 in Fig. 7a) indicates the mutual difference of approximately 15% (as depicted by the shaded yellow area). On the other hand, the results for the calculation with the velocity-dependent friction coefficient (the green solid and black dash-dotted lines in Fig. 7a; see Appendix B, for details) highlight a few observations. First, the penetration depth for the low striking velocities is smaller notably compared to the $\mu = 0.02$ calculation. This is expected, since for these small striking velocities the mean values of the friction coefficients determined (Fig. 7b) are much larger than $\mu = 0.02$ (see also Fig. 9a), which increases the penetration resistance and, consequently, reduces the penetration depth. For example, according to Fig. 7a, at $v_s \approx 800$ m/s the cumulative effect of the friction coefficient exponential reduction—Eq. (29) of Appendix B for

---

[4] The latter results correspond to difference of 17.8% and 17.6%, respectively, if μ is increased from 0.02 to 0.08, which is in good agreement with observations reported in [33] that "a difference up to 25% was noticed when the friction coefficient was varied from 0.02 to 0.1"; see also [34].

$\tau = 200$ m/s—results in equal penetration depth with the $\mu = 0.08$ calculation. (Interestingly, the crossover velocity, $v_s \approx 800$ m/s, corresponds to an order of magnitude smaller friction coefficient $\mu \approx 0.008$ for $\tau = 200$ m/s, according to Fig. 9a.) Also, the penetration depth corresponding to the calculation with $\mu = 0.02$ consistently overestimates the results from the $\mu = f(v_z)$ calculations (up to the highest striking velocities for $\tau = 100$ m/s), which is understandable considering the values of the mean coefficients of friction shown in Fig. 7b.[5] This may, at least formally, suggest the need to use the velocity-dependent friction coefficient in calculations (instead of *any* constant value) due to its cumulative effect *whenever* the penetration process is accompanied by a *significant* change in the value of the coefficient of friction (which could be the case for low-velocity impacts). Unfortunately, a quantitative prediction of the evolution of the friction coefficient corresponding to a specific striking velocity (like those schematized in Fig. 9b) poses a challenge and it is uncertain to what extent is even accessible from experimental measurements.
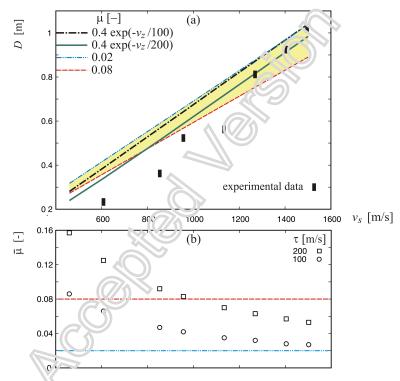

Fig. 7. (a) Comparison of penetration depth calculation results for penetration of a small-size ogive-nose projectile ($m_p = 0.117$ kg, $2a = 12.7$ mm, $\psi=3.0$) into Salem limestone targets obtained under four different treatments of the friction coefficient for the linearized $\bar{\sigma}_r = f(\bar{v}_r)$ dependence (Appendix B). The black rectangles mark the corresponding experimental data (Table 1 of ref. [28]). (b) Mean value of the friction coefficient during the penetration process calculated as $\bar{\mu} = \int_{v_s}^{0} \mu(v_z)\, d v_z \Big/ v_s = \mu_0 \tau \left[\exp\left(- v_s/\tau\right)-1\right]/v_s$ (refer to Appendix B and Eq. (29)).

---

[5] With respect to Fig. 7b, caution should be exercised bearing in mind the discussion in Appendix B. Namely, the functional dependence $\mu = f(v_z)$— hypothetically known based on the experimental data fitting and extrapolation—is likely not usable (in the sense of the path 1 in Fig. 9b) in the course of projectile deceleration ($v_z \to 0$). At the onset of the (high-velocity) penetration, the thin layer of contact surface softens (melts) and μ is reduced (to zero). The corresponding microstructural changes of the interface are irreversible and affect subsequent sliding. Later deceleration of the projectile during penetration may lead to *some* increase in the coefficient of friction which is unlikely to follow the experimentally obtained Eq. (29).

Finally, all four linearized models overestimate the experimentally-obtained penetration depth at low striking velocity (due to the neglect of the quasistatic resistance). At the high striking velocities, the overestimate of the penetration depth is significantly reduced due to the competing effects of the overestimate of the frictional resistance (because the friction coefficient is in reality equal to zero or only slightly higher) and the underestimate of the radial traction (due to the linearized models).

7 Summary

The present study is dedicated to investigation of the penetration depth of long rigid projectiles into the brittle materials susceptible to microcracking. The ogive nose geometry of the projectile is considered as one frequently used and the better suited for the CCE approximation employed herein than the spherical nose geometry. Thus, the functional dependence of the radial traction at the cavity surface on the CCE velocity is stipulated based on the PD simulations. These simulations suggest the mildly nonlinear dependence ($\bar{\sigma}_r \propto \bar{v}_r^\gamma$, $1 < \gamma < 2$) composed on the nonlinear response in the range of extremely low (the quasistatic) and extremely high CCE velocities and only a weakly nonlinear (practically almost linear) response in between. The described PD-driven functional dependence is at the core of the proposed model. This analytical form results in the penetration depth expressions in terms of hypergeometric functions. Consequently, it may be argued that the simplicity of similar empirical formulas is not maintained, which is not convenient for engineering application. Nonetheless, as demonstrated in this analysis, the expressions developed herein are easily evaluated by software systems for modern technical computing (such as, for example, Wolfram Mathematica), while their simplicity rests upon only a few static properties needed (a pair of elastic constants among them) for the estimate.

The approximate model developed based on the key inputs from the PD simulation is validated in the present article against the experimental results for Salem limestone targets and the ogive nose projectiles of three different sizes. These comparisons demonstrate the model capability to predict the penetration depth reasonably well, especially bearing in mind the simplicity of the PD simulations and the fact that the model predictions are based on the mechanical properties obtained under the static loading conditions. However, it is recognized that the proposed model utilizes the indirect (splitting) tensile strength, which is an extrinsic material property, characterized by a large data scatter, and difficult to determine experimentally. The investigation indicate that the one-third reduction of the tensile strength results in the 12% increase of the penetration depth on average, for both small-size and medium-size projectiles, which is considered acceptable. Furthermore, the choice of the exponent γ, which defines the CCE rate dependence of the radial traction at the projectile nose, $\bar{\sigma}_r \propto \bar{v}_r^\gamma$, is proved to be relatively robust in the PD-suggested range of interest, $0 < \gamma \leq 1.5$ within the range of striking velocities that are of practical interest. Arguably the most important parameter choice is that of the friction coefficient. Our simple model in the present form *needs* to include the frictional component in order to reproduce the experimental data. The investigation conducted here draws attention to advantages of using a velocity-dependent friction coefficient in penetration modeling whenever physically justified (presumably, at low impact velocities) and available. In such cases, the use of constant friction coefficient is an iffy proposition since every penetration event is a complex process that encompasses a range of sliding velocities that affect the friction coefficient value. The effect is cumulative and very difficult, if not impossible, to address objectively with the friction coefficient insensitive to the sliding velocity. On the other hand, for the high striking velocities, the irreversible micromechanical and thermomechanical transformations on the contact surface (melting included) render the effect of projectile deceleration on the coefficient of friction largely negligible if not irrelevant. In such cases, the use of frictionless contact is the most physically justified approach.

Finally, the necessity to include frictional resistance in the present model could be alleviated by introducing a correction factor (ranging, for example, from 1.05 to 1.2 depending on the value of the caliber head radius ψ) which would take into account the "sharpness" of the ogive nose and, consequently, the degree of suitability of the CCE approximation.

16

Acknowledgment

This research was supported by the Ministry of Education, Science and Technological Development of the Republic of Serbia.

Declarations

Conflict of interest

The author declares that he has no conflict of interest

Appendix A – Modeling of the radial traction dependence upon the cavity expansion velocity

In the present study, the functional dependence of the radial traction on the CCE radial velocity is assumed in the following form

$$\bar{\sigma}_r = \frac{\sigma_r}{K} = \mathcal{B} + \mathcal{A} \cdot \left(\frac{v_r}{C}\right)^\gamma, \quad \gamma \in \mathfrak{R}^+, \gamma > 1 \tag{15}$$

Based on the results of the CCE PD simulations, the ansatz (15) should satisfy the following four boundary conditions illustrated in Fig. 8:

$$\bar{\sigma}_r\big|_{\bar{v}_r=0} = \left(\bar{\sigma}_r\right)_{st} \tag{16a}$$

$$\frac{d\bar{\sigma}_r}{d\bar{v}_r}\bigg|_{\bar{v}_r=0} = 0 \tag{16b}$$

$$\bar{\sigma}_r\big|_{\bar{v}_r=\alpha\cdot\bar{v}_r^*} = \left(\frac{1-\upsilon}{1+\upsilon}\right)\left(\alpha \cdot \bar{v}_r^*\right) \tag{16c}$$

$$\frac{d\bar{\sigma}_r}{d\bar{v}_r}\bigg|_{\bar{v}_r=\alpha\cdot\bar{v}_r^*} = \left(\frac{1-\upsilon}{1+\upsilon}\right) \tag{16d}$$

The first boundary condition (16a) yields

$$\mathcal{B} = \left(\bar{\sigma}_r\right)_{st} = \sqrt{\frac{3(1-2\upsilon)}{(1+\upsilon)(3-2\upsilon)}\left(\frac{\sigma_f}{K}\right)} \tag{17}$$

The subscript *st* indicates the static solution for the elastic-cracked CCE case, where σ_f designates the indirect tensile strength (the tensile strength corresponding to splitting under the far-field compression rather than tension; also known as, Brazilian tensile strength).

Eq. (15) satisfies the second boundary condition (16b) by definition.

The coupled boundary conditions (16c) and (16d) imply that the curve (15) approaches from above the lower bound given by the inclined line

$$\bar{\sigma}_r^{lb} = \left(\frac{1-\upsilon}{1+\upsilon}\right)\bar{v}_r \tag{18}$$

The parameter $\alpha > 1$ determines the point of contact $\left(\alpha \cdot \bar{v}_r^*\right)$ as indicated by Fig. 8. The transition velocity $\left(\bar{v}_r^*\right)$ is uniquely defined by the intercept of the horizontal line corresponding to the static radial traction, $\left(\bar{\sigma}_r\right)_{st}$ (17), and the inclined line corresponding to the lower-bound radial traction (18). This transition velocity is characterized by the balance of kinetic and potential energies [15].

The remaining boundary conditions (16c) and (16d) could be, respectively, developed as follows

17

$$\left(\overline{\sigma}_r\right)_{st} + \mathcal{A} \cdot \left(\alpha \cdot \overline{v}_r^*\right)^\gamma = \left(\frac{1-\upsilon}{1+\upsilon}\right)\left(\alpha \cdot \overline{v}_r^*\right) \tag{19}$$

$$\mathcal{A} \cdot \gamma \cdot \left(\alpha \cdot \overline{v}_r^*\right)^{\gamma-1} = \left(\frac{1-\upsilon}{1+\upsilon}\right) \tag{20}$$
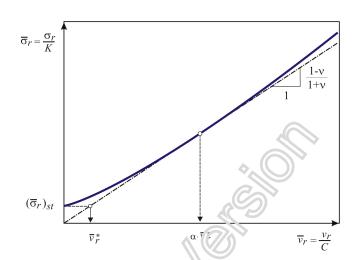

Fig. 8. Schematic representation of the radial traction at the cavity surface vs. CCE velocity. Note that the PD simulation results pinpoint $\overline{v}_r^*$ to 0.0143, which for the Salem limestone used in the numerical example corresponds to 60 m/s. (Interestingly, it has been observed that the narrow range of radial velocities centered on $\overline{v}_r^*$ is characterized by the balance of kinetic and potential energies [15].)

If both sides of Eq. (20) are multiplied by $\alpha \cdot \overline{v}_r^*$, and (15) substituted into the resulting equality, it follows

$$\mathcal{A} \cdot \left(\alpha \cdot \overline{v}_r^*\right)^\gamma = \frac{\alpha}{\gamma}\left(\frac{1-\upsilon}{1+\upsilon}\right)\overline{v}_r^* \quad \Rightarrow \quad \alpha\left(\frac{1-\upsilon}{1+\upsilon}\right)\overline{v}_r^* - \left(\overline{\sigma}_r\right)_{st} = \frac{\alpha}{\gamma}\left(\frac{1-\upsilon}{1+\upsilon}\right)\overline{v}_r^* \tag{21}$$

Since the transitional velocity is defined by the equality

$$\left(\overline{\sigma}_r\right)_{st} = \left(\frac{1-\upsilon}{1+\upsilon}\right)\overline{v}_r^* \tag{22}$$

the relationship between two parameters

$$\gamma = \frac{\alpha}{\alpha - 1}, \quad \alpha > 1 \tag{23}$$

can be readily obtained from Eq. $(21)_2$.

Furthermore, the parameter $\mathcal{A}$ can be expressed from Eq. $(21)_1$

$$\mathcal{A} = \frac{1}{\gamma}\left(\frac{1-\upsilon}{1+\upsilon}\right)\left(\alpha \cdot \overline{v}_r^*\right)^{1-\gamma} \quad \Rightarrow \quad \mathcal{A} = \frac{\alpha^{1-\gamma}}{\gamma}\left(\frac{1-\upsilon}{1+\upsilon}\right)\overline{v}_r^*\left(\overline{v}_r^*\right)^{-\gamma} \tag{24}$$

By substituting Eq. (23) into $(24)_2$ the unknown parameter can be obtained straightforwardly

$$\mathcal{A} = \frac{\alpha^{1-\gamma}}{\gamma}\left(\frac{1-\upsilon}{1+\upsilon}\right)^\gamma\left(\overline{\sigma}_r\right)_{st}^{1-\gamma} = \frac{1}{\gamma}\left(1 - \frac{1}{\gamma}\right)^{\gamma-1}\left(\frac{1-\upsilon}{1+\upsilon}\right)^\gamma\left(\overline{\sigma}_r\right)_{st}^{1-\gamma} \tag{25}$$

The expressions (17), (23) and (25) define parameters of the radial traction (15). An example of these model parameters is presented in Table 3.

Table 3 Example of four sets of model parameters based on PD inputs $v = 0.25$ and $(\overline{\sigma}_r)_{st} = 0.0086$.
(Note that α is selected as the independent parameter. This role is interchangeable with γ.).

α	γ	$\mathcal{A}$
2	2.00	10.47
3	3/2 = 1.50	1.929
4	4/3 = 1.33	1.167
5	5/4 = 1.25	0.928
10	10/9 = 1.11	0.670

Appendix B – Integration of the penetration resistance for $\mu = f(v_z)$

The introduction of the velocity-dependent friction coefficient into the penetration depth calculation presented in Section 5 is not only beset with difficulties regarding necessary inputs but also renders the analytical solution intractable. Consequently, in order to simplify the following analysis, it is assumed henceforth that

$$\overline{\sigma}_r = \overline{\sigma}_r^{lb} = \left(\frac{1-v}{1+v}\right)\overline{v}_r \qquad (26)$$

The assumption (26) neglects: (i) the quasistatic resistance, and (ii) the significant deviation from the linear lower bound (18) in the high-velocity range. Based on Fig. 3, the effect of the first assumption may be considered modest, while the effect of the latter assumption disregarding nonlinearity in the high-velocity region should be more pronounced, especially for the higher striking velocities. Nonetheless, the effects of the simplifying linearization (26) should be examined on case-by-case basis. As an example, Wang and coauthors [42], in their calculation of penetration depth of the rigid projectile into rock, use the linear dependence (26) and estimate the quasistatic-resistance abandon to less than 5% for $v_s \geq 400$ m/s and the influence of the neglect of nonlinearity in the high velocity range to less than 4% for $v_s \leq 1000$ m/s.

Thus, under the assumption (26), the resistance penetration force is obtained as the linear function of the penetration velocity

$$F_z = \lambda_o \left(\alpha_o + \beta_o \, \mu\right)\overline{v}_z \qquad (27a)$$

$$\alpha_o = \frac{1}{2}\sin 2\theta_0 + \arctan\left(\frac{1}{\tan \theta_0}\right) - 2\sin\theta_0 \arctan h(\cos\theta_0) \qquad (27b)$$

$$\beta_o = \frac{2}{3} - \sin\theta_0 \cos^2\theta_0 - \frac{2}{3}\sin^3\theta_0 \qquad (27c)$$

$$\lambda_o = 4\,a^2 \pi \psi^2 \, K\left(\frac{1-v}{1+v}\right) \qquad (27d)$$

The corresponding penetration depth is obtained by integration outlined in Section 5

$$D = \frac{m_p v_s}{\lambda_o \left(\alpha_o + \beta_o \, \mu\right)/C} , \quad \mu = const. \qquad (28)$$

In order to take into account the friction coefficient increase with sliding velocity decrease during projectile deceleration, the following ansatz

$$\mu = \mu_0 \exp\left(-\frac{v_z}{\tau}\right) = \mu_0 \exp\left(-\frac{C\overline{v}_z}{\tau}\right). \qquad (29)$$

19

is introduced and illustrated in Fig. 9a for $\tau = 100$ m/s and 200 m/s and $\mu_0 = 0.4$. The preceding values are selected arbitrarily to facilitate discussion; the evolution of the friction coefficient as a function of loading history is a captivating problem in itself. (Also, note that Eq. (29) neglects, for simplicity, the dependence of the sliding velocity on the penetration velocity: $v_t = v_z \sin\theta$.) The constant values of the friction coefficient, used in Section 6, are marked in Fig. 9a. It can be seen, that the constant μ values of 0.02 (0.08) corresponds to Eq. (28) value for 600 (320) m/s. In other words, for $v_t < 600$ (320) m/s, the friction coefficient exceeds 0.02 (0.08) with exponential rate of increase. On the other hand, at $v_t > 1000$ m/s the friction appears negligible for all practical purposes.
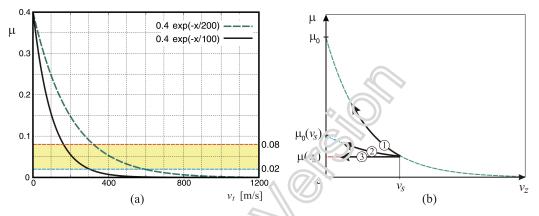

Fig. 9. (a) Assumed friction-coefficient velocity dependence; Eq. (29). (b) Schematics of various variants of the friction coefficient evolution during penetrator deceleration at low striking velocities; with the rise in striking velocity, the sliding friction effect weakens to the extent that it can be ignored

The penetration depth that takes into account the velocity dependent friction, as described above, is

$$D = \frac{m_p\, v_s}{\lambda_o\, \alpha_o\, / C} \left\{ 1 + \frac{1}{(v_s/\tau)} \ln\left(\frac{\alpha_o + \beta_o\, \mu_0\, \exp(-v_s/\tau)}{\alpha_o + \beta_o\, \mu_0} \right) \right\}. \tag{30}$$

where τ and μ_0 are parameters of Eq. (29).

Finally, it seems appropriate to conclude this appendix with reflections on the inherent complexities of the evolution of the friction coefficient depending on the loading history. It is well known that the structure and geometry of the interface between two solid surfaces in contact are of fundamental importance to the phenomenon of friction. The thermomechanisms on the microscale involved with the interfacial failure caused by sliding are extremely complex [44]. The actual contact is established through a myriad of discrete entities (randomly distributed asperities) accounting, cumulatively, to only a small portion of the total nominal area of contact. It cannot be overemphasized that micromechanical and thermomechanical rearrangements of these asperities (and, consequently, the contact interface) during sliding are *irreversible*. Consequently, it should be noted that although assumed functional dependence defined by Eq. (29) can be, in principle, obtained by fitting the dynamic-friction experimental data, the actual evolution of the friction coefficient in the course of projectile deceleration is more complex and not likely to obey such experimentally determined $\mu = f(v_z)$. The reason is that Eq. (29) does not capture the loading history of surfaces involved in the friction contact but is determined by fitting and extrapolating experimental data obtained by a small set of sliding velocities. Namely, if the green dashed line in Fig. 9b represents the experimentally determined Eq. (29), the evolution $\mu = f(v_z)$ following projectile deceleration after the impact with the striking velocity v_s would not likely follow the path 1 during the projectile deceleration (again, especially for high velocity impacts). This is because the high-energy impact leads to rapid, irreversible thermomechanical and chemical changes to the contacting surfaces. In the case of the high striking velocity, a thin layer of material at the projectile nose would melt and act as a lubricant that effectively promotes the frictionless penetration ($\mu = 0$). Even if the melting is not fully

accomplished, the friction coefficient value defined by the striking velocity $\mu = f(v_s)$ in accordance with Eq. (29), may remain largely unchanged for the rest of penetration (the path 3 in Fig. 20). Thus, the friction coefficient evolution paths 1 and 3 represent the upper and the lower bound, respectively, with actual change in reality taking place somewhere in between (the path 2 in Fig. 20). (In that case, the static friction coefficient becomes a function of the entire contact-surface history of change, which is marked in Fig. 9b by $\mu_0 = \mu_0(v_s)$.) It seems reasonable to expect that the higher the striking velocity the closer the path 2 gets to the lower bound (the path 3) with the trend to approach the frictionless penetration, which renders the modeling of friction unnecessary [39].

References

1. Anderson Jr CE (2017) Analytical Models for Penetration Mechanics: A Review. Proc Phys Soc 57: 147–159.

2. Warren TL, Hanchak SJ, Poormon KL (2004) Penetration of limestone targets by ogive-nosed VAR 4340 steel projectiles at oblique angles: experiments and simulations. Int J Impact Eng 30(10):1307-1331.

3. Bishop RF, Hill R, Mott NF (1945) The theory of indentation and hardness tests. Proc Phys Soc 57: 147–159.

4. Kromm A (1948) Zur Ausbreitung von Stosswellen in Kreislochscheiben. Z Angew Math Mech 28: 104-114.

5. Hopkins HG (1960) Dynamic expansion of spherical cavities in metals. In: Progress in Solid Mechanics (Editors I. N. Sneddon and R. Hill), Vol. 1, 83-163. North-Holland, Amsterdam.

6. Goodier JM (1965) On the mechanics of indentation and cratering in solid targets of strain-hardening metal by impact of hard and soft spheres. AIAA: Proceedings of the 7th Symposium on Hypervelocity Impact III: 215–259.

7. Backman ME, Goldsmith W (1978) The mechanics of penetration of projectiles into targets. Int J Eng Sci 16(1): 1-99.

8. Forrestal MJ (1986) Penetration into dry porous rock. Int J Solids Struct 22(12): 1485-1500.

9. Warren TL, Forrestal MJ (1998) Effects of strain hardening and strain-rate sensitivity on the penetration of aluminum targets with spherical-nosed rods. Int J Solids Struct 35: 3737–3753.

10. Masri R, Durban D (2005) Dynamic spherical cavity expansion in an elastoplastic compressible Mises solid. ASME J Appl Mech 72:887–98

11. Kong XZ, Wu H, Fang Q, et al. (2017) Projectile penetration into mortar targets with a broad range of striking velocities: Test and analyses. Int J Impact Eng 106: 18-29.

12. Johnsen J, Holmen JK, Warren TL, Børvik T (2017) Cylindrical cavity expansion approximations using different constitutive models for the target material. Int J Protective Struct 1-27.

13. Zhang Y, Chen W, Cheng S, et al. (2017) Penetration of rigid projectiles into concrete based on improved cavity expansion model. Structural Concrete 1-12.

14. Warren TL (2016) The effect of target inertia on the penetration of aluminum targets by rigid ogive nosed long rods. Int J Impact Eng 91: 6-13.

15. Mastilovic S, Krajcinovic D (1999) High Velocity Expansion of a Cavity within a Brittle Material. J Mech Phys Solids 47: 577-610.

16. Mastilovic S, Krajcinovic D (1999) Penetration of Rigid Projectiles Through Quasi-Brittle Materials. J Appl Mech 66: 585-592.

17. Van Mier JGM (2007) Multi-scale interaction potentials (F − r) for describing fracture of brittle disordered materials like cement and concrete. Int J Fract 143: 41–78.

18. Krajcinovic D, Mastilovic S (1999) Statistical Statistical models of brittle deformation Part I: introduction. Int J Plast 15: 401-426.

19. Rinaldi A, Krajcinovic D, Peralta P, Lai Y-C (2008) Lattice models of polycrystalline microstructures: A quantitative approach. Mech Mater 40: 17–36.

20. Mastilovic S, Rinaldi A (2015) Two-Dimensional Discrete Damage Models: Discrete Element Methods, Particle Models, and Fractal Theories; in: Handbook of Damage Mechanics: Nano to Macro Scale for Materials and Structures, Ed. Voyiadjis G., Springer Science+Business Media, New York. (DOI: 10.1007/978-1-4614-5589-9_23, ISBN 978-1-4614-5588-2), pp. 273-304.

21. Mastilovic S (2008) A Note on Short-Time Response of Two-Dimensional Lattices during Dynamic Loading. Int J Damage Mech 17: 357-361.

22. Rinaldi A (2013) Bottom-up modeling of damage in heterogeneous quasi-brittle solids. Continuum Mech Thermodyn 25(2–4): 359–373.

23. Rinaldi A, Lai YC (2007) Damage theory of 2D disordered lattices: energetics and physical foundations of damage parameter. Int J Plast 23: 1796–1825.

24. Watson E, Steinhauser MO (2017) Discrete Particle Method for Simulating Hypervelocity Impact Phenomena. Materials 10, 379. (DOI:10.3390/ma10040379)

25. Zhou M (2003) A new look at the atomic level virial stress: on continuum-molecular system equivalence. Proc Royal Soc London A 459: 2347–2392.

26. Aomoto K, Kita M (2011) Theory of Hypergeometric Functions, Springer.

27. Kosteski LE, Riera JD, Iturrioz I, Singh RK, Kant T (2018) Assessment of empirical formulas for prediction of the effects of projectile impact on concrete structures. Fatigue Fract Eng Mater Struct 38(8): 948-959.

28. Frew DJ, Forrestal MJ, Hanchak SJ, Green ML (1997) Penetration into Limestone Targets with Ogive-Nose Projectiles. Proceedings of 14th Army Symposium on Solid Mechanics, Myrtle Beach, Battelle Press, SAND96-2494C.

29. Frew DJ, Forrestal MJ, Hanchak SJ (1999) Penetration Experiments with Limestone Targets and Ogive-Nose Steel Projectiles. SAND99-0862J, Sandia National Lab., Albuquerque, NM, USA.

30. Parent T, Domede N, Sellier A, Mouatt L (2015) Mechanical characterization of limestone from sound velocity measurement. Int J Rock Mech Mining Sci 79: 149-156.

31. Nazir R, Momeni E, Armaghani DJ, Amin MF (2013) Correlation between unconfined compressive strength and indirect tensile strength of limestone rock samples. Electron J Geotech Eng 18.1: 1737-1746.

32. Green ML (1992) Laboratory Test on Salem Limestone. Waterways Experiment Station, Viksburg, MS, USA.

33. Crosby ZK (2017) Effects of Thermally Induced Microcracking on the Quasi-Static and Dynamic Response of Salem Limestone. ERDC/GSL TR-17-15. US Army Corps of Engineers, Vicksburg, MS, USA.

34. Ölçmen SM, Jones SE, Weiner RH (2018) A numerical analysis of projectile nose geometry including sliding friction for penetration into geological targets, Proceedings of the Institution of Mechanical Engineers, Part C: J Mech Eng Sci 232 (2): 284-304.

35. Jiang N, Wu S, Hu Y, Mu Z, Wu X, Zhang W (2020) Investigations into the Role of Friction for Rigid Penetration into Concrete-Like Material Targets, Materials 13: 4733.

36. Forrestal MJ, Grady DE (1982) Penetration for Normal Impact into Geological Targets, Int J Solids Struct 18 (3): 229-234.

37. Forrestal MJ, Okajima K, Luk VK (1988) Penetration of 6061-T651 Aluminum Targets With Rigid Long Rods, J Appl Mech 55: 755-760.

38. Chen XW, Li QM (2020) Deep penetration of a non-deformable projectile with different geometrical characteristics. Int J Impact Eng 27: 619–637.

39. Warren TL, Forrestal MJ (1998) Effects of strain hardening and strain-rate sensitivity on the penetration of aluminum targets with spherical-nosed rods. Int J Solids Structures, 35: 3737-3753

40. Hill R (1980) Cavitation and the influence of headshape in attack of thick targets by non-deforming projectiles. J Mech Phys Solids 28: 249-263.

41. Camacho GT, Ortiz M (1997) Adaptive Lagrangian modeling of ballistic penetration of metallic targets. Comput Methods Appl Mech Eng 142: 269-301.

42. Wang MY, Shanbiao Z, Daliang Z (2014) Calculation of depth of projectile penetration into rock. WIT Transactions State of the Art in Sci Eng, 75. doi:10.2495/978-1-84564-879-4/018

43. Rosenberg Z, Vayig Y, Malka-Markovitz A, Kositski R (2021) The penetration of limestone targets by rigid projectiles: Revisited. Int J Protective Structures 12 (1): 110-125.

44. Warren TL, Krajcinovic D (1995) Fractal models of elastic-perfectly plastic contact of rough surfaces based on the Cantor set. Int J Solids Struct 32 (15): 2907-2922.